ELSEVIER

Coordination Chemistry Reviews
198 (2000) 251–263

COORDINATION CHEMISTRY REVIEWS

www.elsevier.com/locate/ccr

P–T phase diagram and Au valence state of the perovskite-type Au mixed-valence complexes $M_2[Au^IX_2][Au^{III}X_4]$ (M = K, Rb, Cs; X = Cl, Br, I)

N. Kojima *, N. Matsushita

Department of Basic Science, Graduate School of Arts and Sciences, University of Tokyo, Komaba 3-8-1, Meguro-ku, Tokyo 153-8902, Japan

Received 18 March 1999; accepted 18 March 1999

Contents

Abstract 251
1. Introduction 252
2. Crystal structure 252
3. P–T phase diagram 254
4. Phase II in $Cs_2Au_2X_6$ and Au^{II} valence state 255
5. Phase III in $Cs_2Au_2X_6$ 258
6. Au valence fluctuation and transport phenomenon 259
Acknowledgements 262
References 263

Abstract

$M_2[Au^IX_2][Au^{III}X_4]$ (M = K, Rb, Cs; X = Cl, Br, I) are perovskite-type gold mixed-valence complexes. In this review, we describe their structural P–T phase diagram, the pressure induced Au valence transition from the $Au^{I,III}$ state to the Au^{II} one, which is coupled with a structural phase transition. The metallic cubic phase appearing under high pressure and high temperature can be obtained as a metastable phase even at ambient pressure and room temperature. In the pressure region below the Au valence transition, $Cs_2[Au^IX_2][Au^{III}X_4]$

* Corresponding author. Tel.: +81-3-5454-6741; fax: +81-3-5454-4311.
E-mail address: cnori@mail.ecc.u-tokyo.ac.jp (N. Kojima)

0010-8545/00/$ - see front matter
PII: S0010-8545(99)00195-2

(X = Cl, Br, I) show metallic behavior, which is attributed to the Au valence-fluctuation.

Keywords: Au complex; Mixed-valence; Valence transition; Perovskite structure; Bipolaron; P–T phase diagram

1. Introduction

Since the discovery of high-Tc superconductors such as $La_{2-x}Ba_xCuO_4$ [1] and $Ba_{1-x}K_xBiO_3$ [2], mixed valence systems having perovskite-type structure have become of great interest. For example, the valence state of Bi has been considered as an important factor for a comprehension of the physical properties of the $BaPb_{1-x}Bi_xO_3$ system. The insulating state of the host compound $BaBiO_3$ is explained by the charge disproportionation of the Bi cations (IV into III and V) which couples to lattice deformation of the stabilization of the commensurate charge density wave. According to recent theory [3], an unusual superconductor is expected due to the Bose condensation of bipolarons under some electron–phonon coupling constant, λ, while in the large limit of λ, a bipolaronic insulator occurs. The insulating $BaBiO_3$ is regarded as an onsite bipolaron system where the bipolarons form a three-dimensional lattice and localize at the Bi^{III} site.

$M_2[Au^IX_2][Au^{III}X_4]$ (M = K, Rb, Cs; X = Cl, Br, I) also have a mixed-valence system having a perovskite-type structure. In this paper, we review their structural P–T phase diagram, the Au valence state, and the physical properties under high pressure.

2. Crystal structure

The crystal structures of $M_2[Au^IX_2][Au^{III}X_4]$ (hereafter referred to as $M_2Au_2X_6$) are shown in Fig. 1. In the crystal, all the halogens are distorted from the midpoint between neighboring Au ions in the Au–X chains, and linear $[Au^IX_2]^-$ and square-planar $[Au^{III}X_4]^-$ complexes occur alternately. Consequently, their structures consist of three-dimensional metal–halogen frame-works formed by elongated octahedra with Au^{III} and compressed octahedra with Au^I sharing their corners. In other words, the breathing-mode-type distortion of AuX_6 octahedra is present in this system. These characteristic properties of crystal structure and mixed-valency are quite similar to those of $BaBiO_3$ which is the parent compound of the superconductors Ba_{1-x}(K or Rb)$_xBiO_3$ and $BaPb_{1-x}Bi_xO_3$. The crystal data and tolerance factor(t) are listed in Table 1 [4–6]. In the cases of $K_2Au_2X_6$ (X = Cl, Br) and $Rb_2Au_2Cl_6$, the synthesis has not yet been reported.

The stability of the perovskite structure (ABX_3) depends on the relative sizes of the A and B elements as well as on the electronic configuration of the B site ions. The size factor is expressed by a tolerance factor(t) obtained by considering the

Table 1
Crystal data and tolerance factor of $M_2Au_2X_6$ (M = K, Rb, Cs; X = CI, Br, I)

Compound	Lattice system	Space group	Unit-cell parameters				t*[a]
			a (Å)	b (Å)	c (Å)	β (°)	
$K_2Au_2I_6$ [4]	Monoclinic	$P2_1/n$	7.283 (3)	9.259(3)	11.587(5)	93.0(1)	0.842
$Rb_2Au_2Br_6$ [5]	Monoclinic	$I2/m$	8.520(1)	7.243(1)	11.210(3)	101.24(5)	0.872
$Rb_2Au_2I_6$	Monoclinic	$I2/m$	8.725 (2)	7.932(1)	11.969(4)	99.53 (2)	0.860
$Cs_2Au_2Cl_6$ [6]	Tetragonal	$I4/mmm$	7.495(1)	$= a$	10.880(2)	90	0.920
$Cs_2Au_2Br_6$	Tetragonal	$I4/mmm$	7.759(1)	$= a$	11.308(1)	90	0.910
$Cs_2Au_2I_6$	Tetragonal	$I4/mmm$	8.284(1)	$= a$	12.092(2)	90	0.895

[a] t* denotes a tolerance factor defined by $R_A + R_X = t\sqrt{2}(R_B + R_X)$, where R_A, R_B, and R_x are the ionic radii of a cation of A-site, another cation of B-site, and an anion, respectively.

structure as derived from a close-packed stacking of the A and X ions. It is generally defined by the relationship $R_A + R_X = t\sqrt{2}(R_B + R_X)$, where R_A, R_B and R_X are the ionic radii. In this relation, the ideal close packing corresponds to $t = 1$. The perovskite structure is found for t values between 0.8 and 1.1. In the case of $Rb_2Au_2X_6$ (X = Br, I) and $K_2Au_2X_6$, because of the small values of t, the crystal structures are distorted into monoclinic and the tilting system of AuX_6 octahedra appears.

3. P–T phase diagram

Fig. 2 shows the P–T phase diagram for $Cs_2Au_2X_6$ (X = Cl, Br, I) [7] and $Rb_2Au_2I_6$ [8]. The mixture of two or three phases in the vicinity of the phase boundary shown in Fig. 2 is due to the nonequilibrium effect and the distribution of pressure and/or temperature in the sample. In the case of $Cs_2Au_2X_6$, two kinds of tetragonal phases and a cubic phase exist. Both the pressure induced phase I(tetragonal)–phase II(tetragonal) transition and the temperature induced phase II–phase III(cubic) transition are of first order. In the case of $Rb_2Au_2I_6$, on the other hand, a monoclinic phase, three kinds of tetragonal phases and a cubic phase exist. In this complex, the pressure induced phase I(monoclinic)–phase II(tetragonal) and phase III(tetragonal)–phase IV(tetragonal) transitions and the temperature induced phase IV(tetragonal)–phase V(cubic) transitions are of first order. For all the complexes in Fig. 2, the cubic phase appearing at high pressures and high temperatures could be obtained as a metastable phase even at room temperature and ambient pressure.

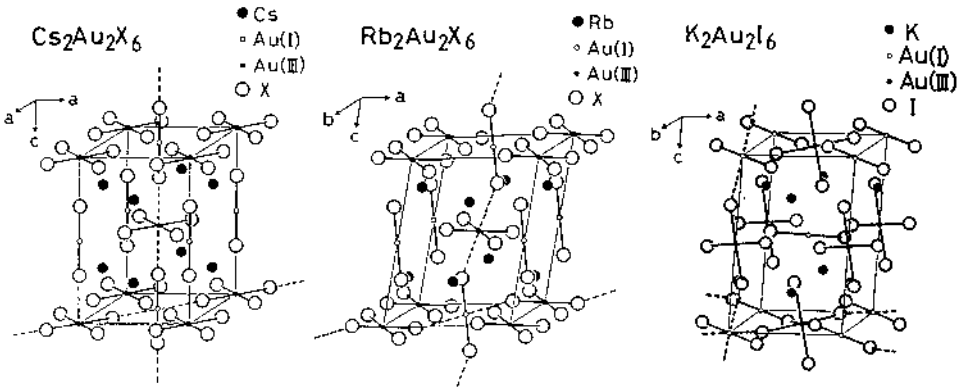

Fig. 1. Crystal structures of $Cs_2Au_2X_6$ (X = Cl, Br, I), $Rb_2Au_2X_6$ (X = Br, I) and $K_2Au_2I_6$.

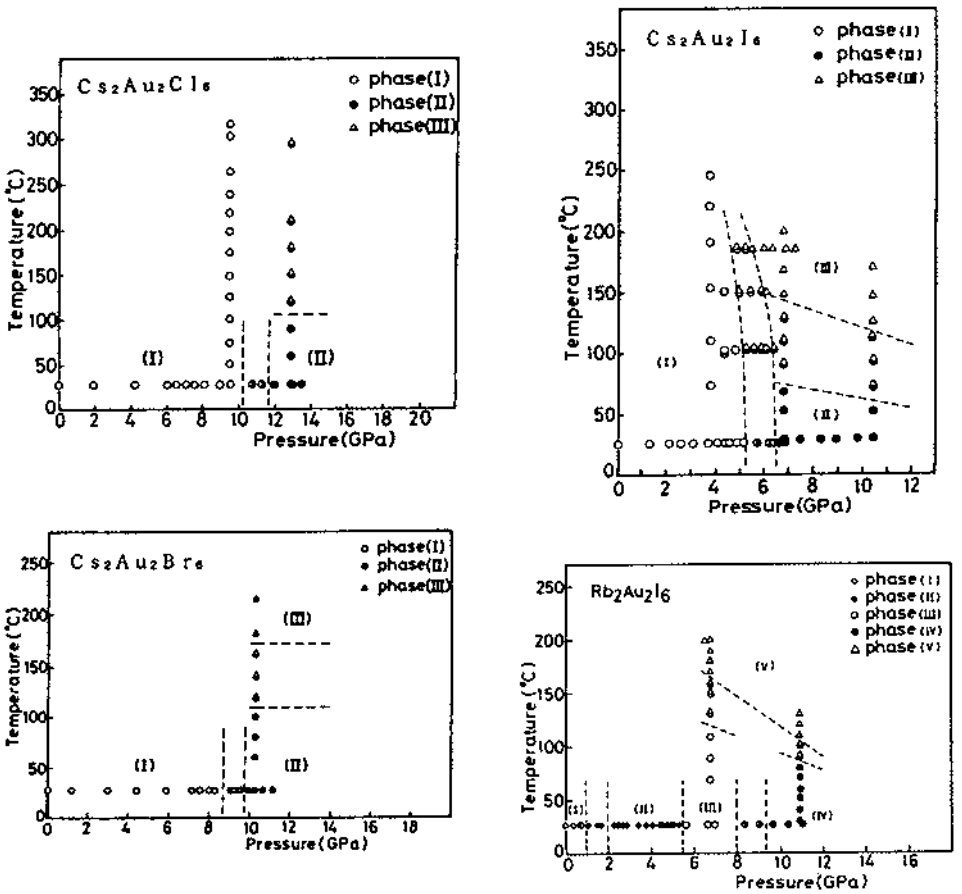

Fig. 2. P–T phase diagrams of $Cs_2Au_2X_6$ (X = Cl, Br, I) and $Rb_2Au_2I_6$. Phases(I, II) and phase(III) in $Cs_2Au_2X_6$ are tetragonal and cubic, respectively. Phase(I), phases(II, III, IV) and phase(V) in $Rb_2Au_2I_6$ are monoclinic, tetragonal and cubic, respectively (from Ref. [7,8]).

4. Phase II in $Cs_2Au_2X_6$ and Au^{II} valence state

At room temperature, $Cs_2Au_2Cl_6$, $Cs_2Au_2Br_6$ and $Cs_2Au_2I_6$ undergo a tetragonal-to-tetragonal phase transition at 11, 9 and 5.5 GPa, respectively [7], whose values are beyond the pressure where the activation energy for the electrical resistivity becomes zero. The pressures where the activation energies become zero are 7.5, 7.2 and 4.4 GPa, for $Cs_2Au_2Cl_6$, $Cs_2Au_2Br_6$ and $Cs_2Au_2I_6$, respectively [9]. Above the pressure where the activation energy becomes zero, the difference between the real oxidation states of Au^{I} and Au^{III} becomes quite small, which is proven by the fact that the (211) and (103) reflections, caused by the distortion of the bridging halogens from the midpoint between the Au^{I} and Au^{III} ions, are hardly detected in this pressure region. If the valence states of Au^{I} and Au^{III} finally become Au^{II} ($5d^9$),

the lowering in symmetry of AuX_6 octahedra should be caused by the Jahn-Teller effect. In the case of $Cs_2Au_2I_6$, when the pressure is applied at room temperature, $2^{1/2}a/c$ increases from 0.969 to 0.980 with increasing pressure up to about 5.5 GPa. However, it drops abruptly from 0.980 to 0.970 at about 5.5 GPa. The abrupt drop in $2^{1/2}a/c$ of $Cs_2Au_2I_6$ is attributed to the band Jahn-Teller transition caused by realization of the Au^{II} valence state.

Above the transition pressure, $2^{1/2}a/c$ of $Cs_2Au_2I_6$ is smaller than 1.0 and decreases with increasing pressure, which implies that the AuI_6 octahedra of $Cs_2Au_2I_6$ are elongated. Considering the distortion of the AuI_6 octahedra in $Cs_2Au_2I_6$, the HOMO in the second tetragonal phase is the half-filled $5d_{x^2-y^2}$. Therefore, the phase II in $Cs_2Au_2I_6$ behaves as a two-dimensional conductor. Fig. 3 shows the electrical resistivities parallel and perpendicular to the c-axis of $Cs_2Au_2I_6$ at 6.5 and 8.0 Gpa [10]. As shown in Fig. 3, the behavior of the conductivity is not an activation type but semimetallic. As expected from the high-pressure X-ray analysis, the behavior of the electrical conductivity in phase II of $Cs_2Au_2I_6$ is highly anisotropic and two-dimensional.

In order to prove the Au valence transition, we have investigated the ^{197}Au Mössbauer spectra of $Cs_2Au_2I_6$ under high pressures up to 12.5 GPa [11] (Fig. 4). The valence states of Au^{I} and Au^{III} at ambient pressure are clearly distinguishable. In connection with peak assignment, a best fit in Fig. 4 is obtained with two doublets, the outer with lower intensity being assigned to Au^{I}, the inner to Au^{III}. The isomer shifts of Au^{I} and Au^{III} sites at 0.0 GPa are -0.09 and 0.50 mm s^{-1}, respectively, and the quadrupole splittings of Au^{I} and Au^{III} are 4.63 and 1.71 mm s^{-1}, respectively. This assignment is the same as that in Ref. [12], but different from that in Ref. [11]. In our present assignment, the two doublets are nested, i.e. the Au^{III} doublet is inside the Au^{I} doublet. However, in Ref. [11], the two doublets are side by side. In Ref. [11], the quadrupole splittings of Au^{I} and Au^{III} in $Cs_2Au_2I_6$ are 3.69 and 2.33, which is quite different from those of Au^{I} and Au^{III} complexes (e.g. $[Bu_4N][AuI_2]$ and $KAuI_4$), respectively.

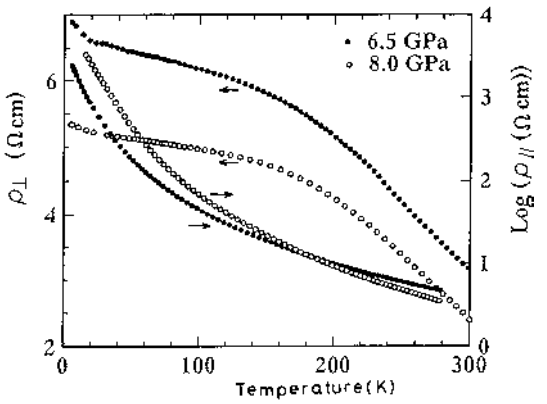

Fig. 3. Temperature dependence of the electrical resistivity parallel and perpendicular to the c-axis of $Cs_2Au_2I_6$ at 6.5 GPa and 8.0 GPa (from Ref. [10]).

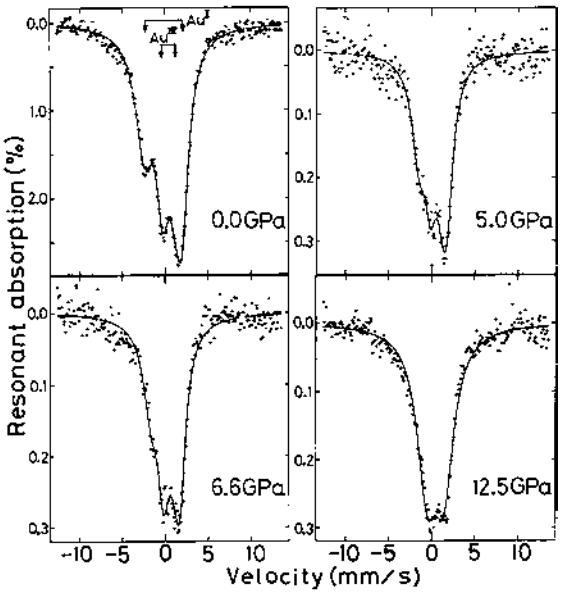

Fig. 4. ^{197}Au Mössbauer spectra of $Cs_2Au_2I_6$ at several pressures (from ref.[11]). $T = 4.2$ K. Isomer shift is relative to gold in platinum. The spectrum at 12.5 GPa shows one doublet assigned to Au^{II}.

As shown in Fig. 4, with increasing pressure, a gradual increase in the overlap of the doublets is observed due to a substantial increase of the isomer shift (IS) of Au^{I} and a less pronounced decrease of that of Au^{III} with increasing pressure. Finally, the ^{197}Au Mössbauer spectrum at 12.5 GPa shows only one electronic state for Au in $Cs_2Au_2I_6$. Therefore, the Au valence state of the tetragonal(II) phase in $Cs_2Au_2I_6$ is Au^{II}, which is the first direct observation of the Au^{II} state in a relatively simple, primarily ionic compound.

In connection with phase II in $Cs_2Au_2Cl_6$, the single crystal X-ray diffraction measurement under high pressures was measured by Denner et al. for the first time [13]. According to them, with increasing pressure the Cl ions shift gradually toward the midpoint of the Au ions which is attained at 5.2 GPa. Therefore, they described that the Au sites become indistinguishable and the valence state of Au is Au^{II} above 5.2 GPa. However, ^{197}Au Mössbauer spectra [14,15] and Raman spectra [16] of $Cs_2Au_2Cl_6$ under high pressures have shown that the Au^{I} and Au^{III} states are clearly distinguishable even at 6.8 and 8.0 GPa. Recently, we have performed the single crystal X-ray diffraction for $Cs_2Au_2Cl_6$ under high pressures up to 18 GPa by using He gas as a pressure medium [17], and have detected the superstructure reflections (hkl; l = odd) due to the shift of the Cl ions from the midpoint of the Au ions even at 12.0 GPa. These superstructure reflections disappeared at the phase I–phase II transition ($P = 12.5$ GPa). As shown in Fig. 5, at about 12.5 GPa, the lattice parameters a and c approach each other, resulting in the relation $2^{1/2}a = c$. The crystal structure changes from tetragonal ($I4/mmm$) to cubic ($Pm3m$) at about

12.5 GPa. This result is not consistent with that of the previous powder X-ray diffraction measurement [7]. According to the powder X-ray diffraction measurement, $Cs_2Au_2Cl_6$ undergoes a tetragonal-to-tetragonal phase transition at about 11 GPa and room temperature, and undergoes a tetragonal-to-cubic phase transition above 12 GPa and 100°C. The cubic phase exists at room temperature under high pressures on condition that He gas is used as an ideal hydrostatic pressure medium. In the case of the previous powder X-ray diffraction measurement, the pressure medium was kerosene which is not a good hydrostatic medium under high pressure, and shearing stress might be responsible for the appearance of the second tetragonal phase in $Cs_2Au_2Cl_6$. The structural pattern of the phase II in $Cs_2Au_2X_6$ is sensitive to the kind of pressure medium.

5. Phase III in $Cs_2Au_2X_6$

Now, we investigate the relationship between the phase II–phase III transition and the behavior of the resistivity. According to our resistivity measurement of $Cs_2Au_2I_6$ under high pressures [9], $Cs_2Au_2I_6$ undergoes a pressure-induced semiconductor-to-metal transition at 4.5 GPa and room temperature. Moreover, as shown in Fig. 6a [9], when the temperature is increased at 6.5 GPa, the resistivity decreases and a steep drop occurs at about 300 K and then increases linearly above about 400 K. Comparing the behavior of the resistivity with the X-ray diffraction profiles in the vicinity of the tetragonal-to-cubic phase transition, the drastic resistivity drop at about 300 K and the linear increase in the resistivity above 400 K are attributed to the beginning and the end of the phase transition, respectively. In the cooling process, the resistivity decreases linearly with temperature cooled down to room

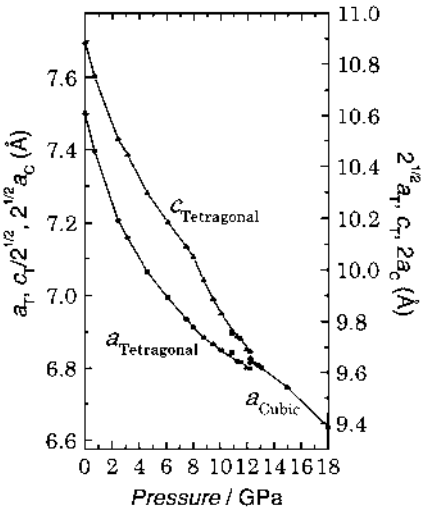

Fig. 5. Pressure dependence of unit cell parameters of $Cs_2Au_2Cl_6$ at room temperature (from Ref. [17]).

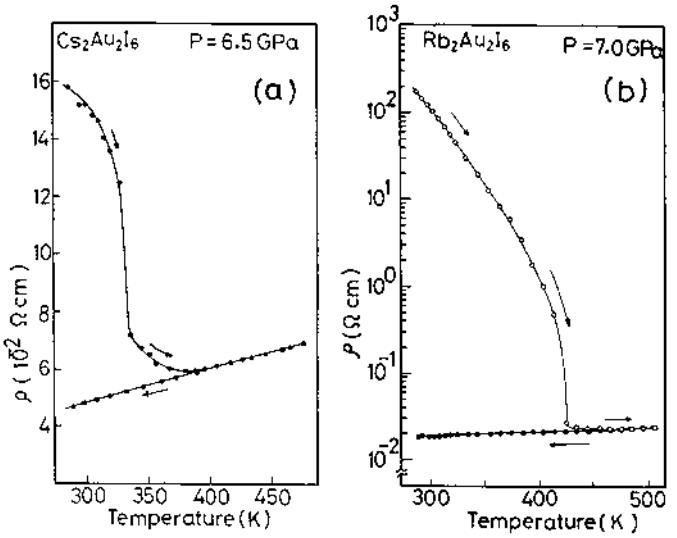

Fig. 6. (a) Temperature dependence of the resistivity of $Cs_2Au_2I_6$ at 6.5 GPa (from Ref. [9]). The sample was first heated up to 470 K, then cooled down to room temperature. (b) Temperature dependence of the resistivity of $Rb_2Au_2I_6$ at 7.0 GPa (from Ref. [8]). The sample was first heated up to 510 K, then cooled down to room temperature.

temperature, which implies that the cubic phase can be stable at 6.5 GPa and room temperature. Moreover, this metallic phase could be obtained as a metastable phase at ambient pressure and room temperature by decreasing temperature and pressure after increasing pressure up to 6.5 GPa and temperature up to 470 K [9]. Fig. 7 shows the X-ray powder pattern of the metastable phase of $Cs_2Au_2I_6$ [9], which implies that the metallic metastable phase is a cubic perovskite structure.

Fig. 6b shows the resistivity of $Rb_2Au_2I_6$ as a function of temperature at 7.0 GPa [8]. The steep drop in the resistivity at about 420 K is due to the tetragonal(III)-to-cubic transition. As shown in Fig. 6b, the metallic phase is stable at 7.0 GPa and room temperature in the cooling process. Moreover, this metallic phase could be obtained as a metastable phase at ambient pressure and room temperature.

6. Au valence fluctuation and transport phenomenon

Fig. 8 shows the temperature dependence of the electrical resistivity of $Cs_2Au_2Cl_6$ under the pressure region below the Au valence transition (11–12 GPa) [18]. At 5 GPa, a gradual semiconductor-to-metal transition occurs about 250 K. With decreasing temperature, the resistivity decreases slowly from 250 to 100 K and then increases below 100 K. At 6 GPa, the metallic region is spread between 250 and 5 K. Under the pressure region above 7 GPa, the resistivity as a function of temperature is metallic in the whole measurement temperature region.

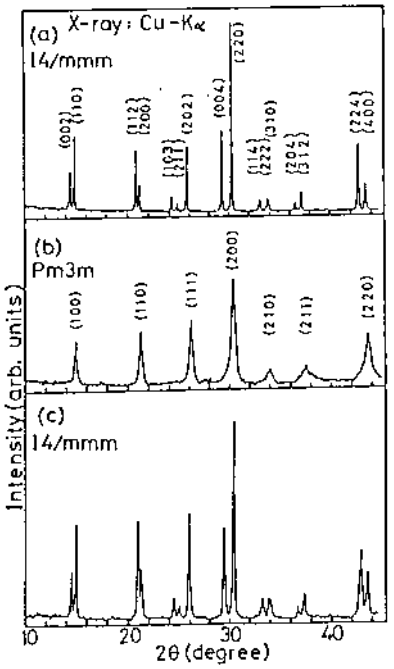

Fig. 7. X-ray powder patterns of $Cs_2Au_2I_6$ at room temperature and ambient pressure (from Ref. [9]). (a) X-ray pattern before applying pressures. (b) X-ray pattern of the metastable phase obtained by decreasing temperature and pressure after increasing pressure up to 6.5 GPa and increasing temperature up to 480 K. (c) X-ray pattern after annealing the metastable phase at 370 K.

According to the ^{197}Au Mössbauer spectra of $Cs_2Au_2Cl_6$ [14], which is shown in Fig. 9, the Au^{I} and Au^{III} states are clearly distinguishable even at 6.8 GPa (= 68 kbar). The spectral profile at 4.2 K and 6.8 GPa resembles closely that at 4.2 K and

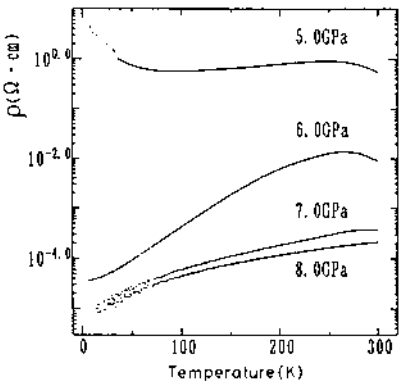

Fig. 8. Temperature dependence of the electrical resistivity perpendicular to the c-axis of $Cs_2Au_2Cl_6$ (from Ref. [18]).

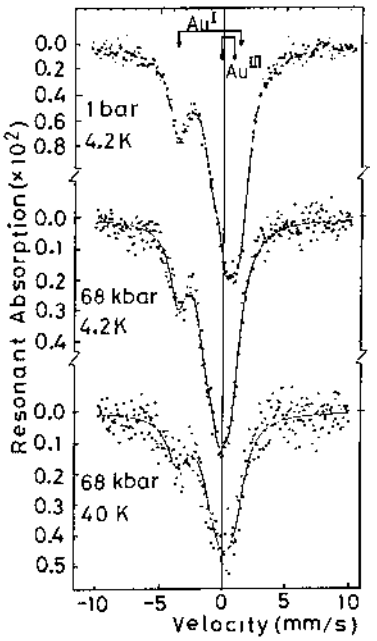

Fig. 9. ^{197}Au Mössbauer spectra of $Cs_2Au_2Cl_6$ at ambient pressure and 68 kbar (from Ref. [14]).

0.0 GPa, which strongly proves that the metallic behavior in the phase I of $Cs_2Au_2Cl_6$ is most likely attributed to the dynamic two-electron exchange between Au^I and Au^{III} sites (i.e. highly mobile bipolaron) (Fig. 9).

Fig. 10 shows the temperature dependence of the electrical resistivity of $Cs_2Au_2I_6$ under the pressure region below the Au valence transition (5.5 GPa) [18]. Several anomalous peaks and shoulders appear at about 210 and 130 K (Fig. 10). However,

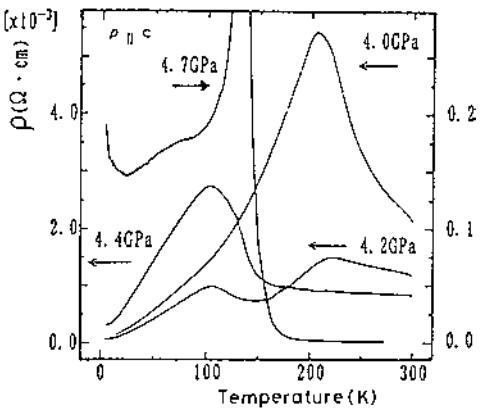

Fig. 10. Temperature dependence of the electrical resistivity parallel to the *c*-axis of $Cs_2Au_2I_6$ (from Ref. [18]).

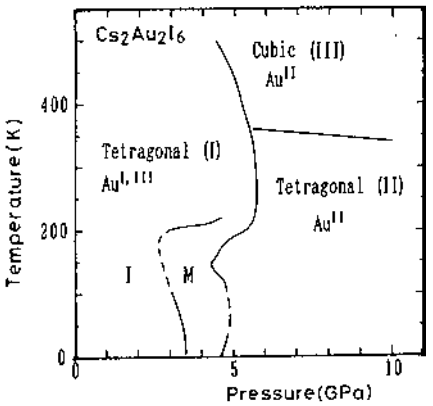

Fig. 11. P–T phase diagram of $Cs_2Au_2I_6$ (from Ref. [18]). I and M in the tetragonal(I) phase indicate the insulating and metallic phases, respectively.

above the Au valence transition, no anomalous resistivity peak is observed at all [10]. The origin of the resistivity peak at about 210 K in the pressure region between 3.0 and 4.2 GPa is presumably the same as that of the resistivity peak about 250 K for $Cs_2Au_2Cl_6$ in the pressure region between 5 and 6 GPa. On the other hand, the resistivity peak at about 130 K appears above 4.5 GPa, and is strikingly enhanced as the pressure approaches the Au valence transition. Apparently, the resistivity anomalies around 130 and 210 K are successive and complementary. However, considering that any successive anomalous resistivity peak is not observed for $Cs_2Au_2Cl_6$, the resistivity anomalies around 130 and 210 K for $Cs_2Au_2I_6$ are independent of each other. At 4.7 GPa, the value of the resistivity peak at 130 K is quite similar to that of the second tetragonal phase. Therefore, the resistivity anomaly at 130 K for $Cs_2Au_2I_6$ is attributed to the re-entrant phenomenon of the metallic phase I.

Consequently, in the case of $Cs_2Au_2I_6$, the electrical resistivity as a function of temperature shows a re-entrant phenomenon of the metallic bipolaron phase in the vicinity of the Au valence transition. Fig. 11 shows the P–T phase diagram of $Cs_2Au_2I_6$ determined from the X-ray diffraction pattern and resistivity under high pressures.

Acknowledgements

The authors wish to thank collaborators, Dr H.Kitagawa of JAIST, Professor S.S. Hafner, Dr Li Zhang and Dr H. Ahsbahs of the University of Marburg, Dr J. Stanek of Jagiellonian University, Professor N. Mori of the University of Tokyo, Professor H. Takahashi of Nihon University, Professor O. Shimomura of Japan Atomic Energy Research Institute, and Dr T. Kikegawa of High Energy Accelerator Research Organization (KEK). N. Kojima was supported by a Grant-in-Aid for Scientific Research from the Ministry of Education, Science and Culture, Japan.

References

[1] J.G. Bednorz, K.A. Müller, Z. Phys. B64 (1986) 189.
[2] R.J. Cava, B. Batlogg, J.J. Krajewski, R. Farrow, L.W. Rupp Jr., A.E. White, K. Short, W.F. Peck, K. Kometani, Nature 332 (1988) 81.
[3] (a) B.K. Chakraverty, J. Phys. Lett. 40 (1979) L99. (b) A. Alexandrov, J. Ranninger, S. Robaszkiewicz, Phys. Rev. B33 (1986) 4526. (c) D. Emin, M.S. Hillery, Phys. Rev. B39 (1989) 6575.
[4] J. Strähle, J. Gelinek, M. Kolmel, A.M. Nemecek, Z. Naturforsch. 34b (1979) 1047.
[5] J. Strähle, J. Gelinek, M. Kolmel, Z. Allg. Chem. 456 (1979) 241.
[6] (a) J.C.M. Tindemans-v. Eijndhoven, G.C. Verschoor, Mater. Res. Bull. 9 (1974) 1667. (b) N. Matsushita, H. Kitagawa, N. Kojima, Acta Crystallogr. C53 (1997) 663.
[7] N. Kojima, M. Hasegawa, H. Kitagawa, T. Kikegawa, O. Shimomura, J. Am. Chem. Soc. 116 (1994) 11368.
[8] N. Kojima, Mol. Cryst. Liq. Cryst. 285 (1996) 295.
[9] N. Kojima, H. Kitagawa, T. Ban, F. Amita, M. Nakahara, Synth. Met. 41–43 (1991) 2347.
[10] H. Kitagawa, N. Kojima, H. Takahashi, N. Môri, Synth. Met. 55–57 (1993) 1726.
[11] S.S. Hafner, N. Kojima, J. Stanek, L. Zhang, Phys. Lett. A192 (1994) 385.
[12] H. Kitagawa, N. Kojima, H. Sakai, J. Chem. Soc. Dalton Trans. (1991) 3211.
[13] W. Denner, H. Schulz, H. D'Amour, Acta Crystallogr. A35 (1979) 360.
[14] J. Stanek, S.S. Hafner, H. Schulz, Phys. Lett. A76 (1980) 333.
[15] J. Stanek, J. Chem. Phys. 76 (1982) 2315.
[16] H. Tanino, K. Syassen, Z. Wang, M. Hanfland, K. Takahashi, High Press. Res. 3 (1990) 183.
[17] N. Matsushita, H. Ahsbahs, S.S. Hafner, N. Kojima, Rev. High Press. Sci. Technol. 7 (1998) 329.
[18] N. Kojima, F. Fukuhara, H. Kitagawa, H. Takahashi, N. Môri, Synth. Met. 86 (1997) 2175.